

Screening of Filler Material for a Packed-Bed Thermocline Energy Storage Test Facility with Lead–Bismuth Eutectic as the Heat Transfer Fluid

Franziska Müller-Trefzer,* Annette Heinzl,* Robin Hesse, Alfons Weisenburger, Thomas Wetzel, and Klarissa Niedermeier

Suitable solid filler materials are investigated for use in a packed-bed heat storage test facility for high temperatures with lead–bismuth eutectic (LBE) as the heat transfer fluid. Accordingly, first, the thermophysical properties of six different candidate materials, two glasses and four ceramics, are determined. The density and heat capacity are measured experimentally and the thermal conductivity is discussed based on literature data. Subsequently, a static corrosion test is performed at 500 °C for 1 and 4 weeks in LBE under reducing conditions. The glasses are found to be unsuitable due to corrosion attack. Among the ceramics, zirconium silicate and zirconium oxide are identified to be highly resistant to corrosion. Zirconium silicate is subsequently also successfully tested as a storage material in a laboratory experiment under cyclic conditions.


1. Introduction

Energy storage is the key for a successful transition to larger renewable energy shares. It enables the decoupling of energy supply and demand in time and, thus, integrates larger shares of fluctuating energy sources. One possibility is to store the fluctuating energy, for example, from renewable electricity sources

F. Müller-Trefzer, R. Hesse, T. Wetzel, K. Niedermeier
Institute for Thermal Energy Technology and Safety (ITES)
Karlsruhe Institute of Technology (KIT)
Hermann-von-Helmholtz-Platz 1, Eggenstein-Leopoldshafen 76344,
Germany
E-mail: Franziska.mueller-trefzer@kit.edu

A. Heinzl, A. Weisenburger
Institute for Pulsed Power and Microwave Technology (IHM)
KIT
Hermann-von-Helmholtz-Platz 1, Eggenstein-Leopoldshafen 76344,
Germany
E-mail: annette.heinzl@kit.edu

T. Wetzel
Institute of Thermal Process Engineering (TVT)
KIT
Kaiserstraße 12, Karlsruhe 76131, Germany

 The ORCID identification number(s) for the author(s) of this article can be found under <https://doi.org/10.1002/ente.202300781>.

© 2023 The Authors. Energy Technology published by Wiley-VCH GmbH. This is an open access article under the terms of the Creative Commons Attribution License, which permits use, distribution and reproduction in any medium, provided the original work is properly cited.

DOI: 10.1002/ente.202300781

(power to heat)^[1] or concentrated solar power plants (solar process heat),^[2] in the form of heat for use as process heat in industrial processes or for electricity generation. In the case of electricity generation, heat at a high-temperature level is advantageous, as the Carnot efficiency increases with increasing temperature. Furthermore, high-temperature heat can also be used directly for providing process heat at a high-temperature level. In the European Union, for example, process heat of 2000 TWh year⁻¹ is needed.^[3,4]

The most mature high-temperature (>300 °C) thermal energy storage (TES) technologies are two-tank heat storage systems with molten salt, which are commercially applied in concentrated solar power plants,^[3,4] and solid storage systems with gases or oil as heat transfer fluids (HTFs).^[1,5–7] The performance of these storage systems is limited by a low heat transfer coefficient in the case of gaseous HTFs, such as air, and the decomposition temperature in the case of liquid HTFs, such as oil and molten salt. The maximum operating temperature of solar salt (NaNO₃:KNO 60:40 wt%), for example, is limited to a temperature of about 600 °C.^[8]

Liquid metals are promising alternative HTFs for high-temperature TES,^[9–12] as liquid metals exhibit excellent heat transfer properties and are chemically stable in a wide-temperature range. Safety aspects need to be considered. They are, however, well known because of their use in the nuclear industry.^[13] They do not qualify for direct heat storage because of their relatively high cost, which is why a packed-bed TES is being investigated.^[14] The HTF proposed here, lead–bismuth eutectic (LBE), has a melting point of 124.8 °C and can be used up to temperatures above 1000 °C.^[12] The authors' previous theoretical investigations have shown that a thermocline packed-bed storage configuration with liquid metal as the HTF is a promising option for high-temperature TES.^[14] Its technical operability on a lab scale was successfully demonstrated at the Karlsruhe Liquid Metal Laboratory (KALLA).^[15]

However, a major challenge when working with liquid metal is its corrosiveness, which increases with rising temperature.^[16,17] Liquid metals can dissolve elements of solid structural material, form intermetallic compounds, or penetrate into the solid structure, leading to a change in the mechanical properties.

Corrosion of steels by LBE has been investigated intensively and diversely.^[12] Materials for piping, tanks, and instrumentation are known and have been proven in liquid LBE up to 550 °C, and further research is ongoing for higher temperatures.^[18,19] However, there is very little research reported in the literature on the compatibility of materials with LBE that can potentially be used as packed-bed storage material.

As a first step toward the demonstration of a high-temperature TES with liquid metal, this article presents the selection procedure of suitable filler material for temperatures up to 500 °C. The most promising material will then be tested in a first packed-bed experiment in an existing test loop at KALLA, which is limited to 450 °C, and the results concerning the filler material of the packed bed will be presented and discussed. Furthermore, the temperature measuring technique in a packed-bed TES with LBE will be tested and important design parameters can be derived for larger-scale systems, which is discussed in more detail in ref. [15]. In parallel, material tests (both structural and filler material) for higher temperatures beyond 700 °C will be currently performed, but are not part of this study.

This article is organized in two parts. The methodology and the results for the physical properties of the potential filler materials that are relevant for the performance of a packed-bed thermocline heat storage, such as density, heat capacity, and thermal conductivity, are shown in the first part (Characterization of Physical and Thermophysical Properties). In the second part (Static Corrosion Tests), the methodology and the results for the static corrosion tests in LBE at 500 °C to investigate the compatibility of the packed materials with LBE are presented. Finally, the results of testing one of the selected materials in a lab-scale TES for 37 cycles between 180 and 380 °C are discussed to assess the thermal cycling behavior of the filler material.

2. Selection of Potential Filler Material Based on Literature Data

Based on the target application of the materials investigated as a filler in a packed-bed TES, the materials should have a high volumetric heat capacity, low thermal conductivity, high thermal fatigue, and thermal shock resistance, need to be compatible with LBE, and should be low cost, which is explained in more detail in the study by Müller-Trefzer et al.^[15] The most important criteria for the selection of filler materials are the thermophysical properties and material compatibility. As there are very few data^[11,20,21] available regarding the operation of a packed-bed TES with liquid metals as the HTF, a well-defined packed bed was intended to be tested for validation purpose. The porosity distribution is very predictable for a packed bed consisting of monodisperse spheres or spheres with a narrow particle size distribution, and the behavior of this type of packing has already been described manifold in the literature.^[22,23]

A selection of potential filler materials, which exhibit the thermophysical properties mentioned and are offered as spherical particles, can be classified into two categories.

Glasses	Ceramics
Diamond Pearls ($d = 8$ mm)	Aluminum oxide (90%) ($d = 2.5$ – 3 mm)
Borosilicate glass ($d = 9$ mm)	Steatite C220 ($d = 10$ mm)
	Zirconium oxide (yttrium-stabilized) ($d = 10$ mm)
	Zirconium silicate (Rimax) ($d = 2.5$ – 2.8 mm)

Even though natural stones are an interesting option in terms of costs, they were not investigated in this study because they did not fulfill the geometric requirements for the planned experiments of using them as filler material in thermal heat storage, as described above. In addition, their thermophysical properties, such as volumetric heat capacity and thermal conductivity, are subject to much greater natural variations than commercially produced glasses or ceramics. However, due to their cost advantages, natural stones may still be considered and investigated further in the future.

3. Characterization of Physical and Thermophysical Properties

The heat capacity and density of the storage material characterize the volumetric heat capacity, which should be as large as possible to enable a compact storage realization. The thermal conductivity of the storage material influences the effective thermal conductivity in the TES and, thus, the efficiency of the charging and discharging process, on the one hand, and the stability of the thermocline during the standby state, on the other hand.

3.1. Methodology for the Determination of the Thermophysical Properties Selected

3.1.1. Density (ρ)

The density was determined with a gas pycnometer, Micro-Ultrapyc 1200e (Quantachrome Instruments) with an accuracy of measurement of 2.5–5%. The gas pycnometer used here operates on the principle of volumetric displacement.

The measurements were performed by the Institute of Thermal Process Engineering (TVT, Karlsruhe Institute of Technology: KIT) with two different purge gases (nitrogen and helium). The device determines the density of a sample several times until the last three measurements do not differ more than 0.05%. The density was given as an average of these last three measurements and determined three times independently for each material sample, and the results were then averaged. The standard deviation of the values measured was always less than 0.6%, which shows the good repeatability of the measurements.

3.1.2. Specific Heat Capacity (c_p) and Temperature Limitation of the Filler Materials

The specific heat capacity was determined with a differential scanning calorimetry (DSC) 404 F1 Pegasus (Netzsch) from room temperature up to 1000 °C for the ceramics and up to the melting region for the glasses, since melting of the glasses was expected to take place significantly below 1000 °C. The manufacturer states a maximum measurement uncertainty of 3%.

A heating rate of 20 K min^{-1} was applied. Argon was used as a purge gas and sapphire was used as the calibration standard.

A maximum size of 5 mm in diameter and 1–2 mm in height was required for the heat capacity measurement. Therefore, the material was embedded in a resin cured by ultraviolet light (Technovit 2000 LC, Kulzer GmbH, Mitsui Chemicals) and ground to the size desired. In the end, the resin was removed with the help of acetone.

3.1.3. Thermal Conductivity (λ)

The thermal conductivity depends strongly on the microstructure of the material, which is influenced by the composition. Furthermore, the porosity reduces the effective thermal conductivity compared to a 100% dense material. There are several experimental methods and commercial apparatuses used to determine the thermal conductivity of TES material, such as the laser flash analyzer, transient hot-wire method, guarded hot plate, or a heat flow meter.^[24] However, all these methods either require larger sample geometries than can be produced from commercially available sphere sizes investigated here or cannot be used at temperatures up to $500 \text{ }^\circ\text{C}$. Our own production of larger samples corresponding to the commercial spheres is not possible due to the lack of information on the production process. Therefore, a literature review was conducted instead.

3.2. Results of the Determination of the Thermophysical Properties

3.2.1. Density (ρ)

The densities determined by the method described in Section 3.1.1 are given in Table 1.

The density determined with helium as the purge gas is slightly higher than that determined with nitrogen. This observation could be due to the dissimilar adsorption behavior of the different gas molecules on the surface. However, it is also possible that small pores are penetrated better by small gas molecules.

Table 1. The density and standard deviation of potential filler material samples measured at about $23 \text{ }^\circ\text{C}$ as well as corresponding data from the supplier and, for comparison, the density of LBE at 200 and $1000 \text{ }^\circ\text{C}$ from literature data are given.

Material	ρ_{N_2} [kg m^{-3}]	T [$^\circ\text{C}$]	ρ_{He} [kg m^{-3}]	T [$^\circ\text{C}$]	$\rho_{\text{literature}}$ [kg m^{-3}]	References
Diamond Pearls	2541 ± 3	23.1	2545 ± 1	22.8	2500 ± 40	[50]
Borosilicate glass	2180 ± 12	23.1	2208 ± 6	22.9	2230	[26]
Al_2O_3 (90%)	3570 ± 12	23.2	3584 ± 8	22.9	3630 ± 70	[52]
Steatite	2630 ± 12	23.2	2653 ± 2	22.8	>2550	[55]
Zirconium silicate (Rimax)	4224 ± 8	23.1	4235 ± 2	22.9	4100	[62]
Zirconium oxide	5982 ± 1	23.1	6004 ± 10	23.0	6020	[59]
LBE	–	–	–	200	$10\,453^{\text{a}}$	[12]
				1000	9419^{a}	

^aCalculated with $\rho_{\text{LBE}}/(\text{kg m}^{-3}) = 11065 - 1.293 \cdot T/\text{K}$.^[12]

The molecular size of nitrogen is about 0.3 nm, whereas that of helium is about 0.2 nm.^[25] Helium molecules could, therefore, penetrate better into very small pores, resulting in a larger penetration volume and, thus, a smaller sample volume, which increases the value for the density. Consequently, the density determined with helium is used in the following sections.

The densities measured align closely with those of the manufacturers' specifications and never deviate by more than 3.2% from each other, except for steatite, where the deviation is about 3.9%. Only a minimum density for steatite is specified by the manufacturer.

3.2.2. Specific Heat Capacity (c_p)

The measurements were determined by the Netzsch measurement services, and the temperature-dependent heat capacity (c_p) is given in Figure 1.

It should be emphasized here that no clear melting regions (endothermic effects) above the glass transition temperatures were detected for the glass samples; however, bubble formation within the samples was detected after the measurement. Thus, a partial decomposition or phase transition must have taken place, but this could not be clearly detected by DSC.

The results of the measurements are shown in Table 2 with data from literature for similar materials where available. The data measured are in good accordance with data from the literature, which are also shown in Table 2. Only the heat capacity for zirconium silicate, determined by DSC, differs from the data given by the manufacturer, but agrees well with the data given in the literature.

The DSC measurements showed a glass transition for the Diamond Pearls starting at about $540 \text{ }^\circ\text{C}$ and ending at $570 \text{ }^\circ\text{C}$, which agrees well with the deformation temperature of $575 \text{ }^\circ\text{C}$ specified by the manufacturer.

A glass transition was also detected for borosilicate glass with an onset at about $550 \text{ }^\circ\text{C}$ and an end of about $610 \text{ }^\circ\text{C}$. These findings agree well with the manufacturer's specifications of a glass transition temperature of $525 \text{ }^\circ\text{C}$ for the glass spheres.^[26]

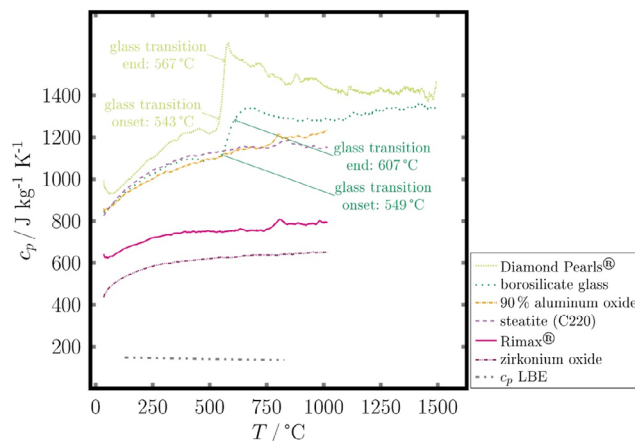


Figure 1. Heat capacity (c_p) depending on temperature (T) measured by DSC 404 F1 Pegasus (Netzsch) for different material samples, except for the heat capacity of LBE, which was calculated by the equation given in Table 2.

Table 2. Data of the heat capacity of potential filler material determined with a Netzsch DSC 404 F1 Pegasus and from literature and the heat capacity for LBE at 130 and 820 °C is given for comparison.

Material	c_p [J kg ⁻¹ K ⁻¹]	$c_{p,literature}$ [J kg ⁻¹ K ⁻¹]	References
Diamond Pearls	941 _{T=50 °C} –1420 _{T=1400 °C} ^{a)}	n.a.	–
Borosilicate glass	855 _{T=50 °C} –1346 _{T=1400 °C} ^{a)}	n.a.	–
Al ₂ O ₃ (90%)	855 _{T=50 °C} –1226 _{T=1000 °C}	755–785 _{RT} ^{b)} 850–1050 _{T=30–1000 °C}	for 86–94.5% Al ₂ O ₃ [45] for 86–95% Al ₂ O ₃ [63]
Steatite	852 _{T=50 °C} –1151 _{T=1000 °C}	800–900 _{T=30–600 °C}	[63]
Zirconium silicate (Rimax)	626 _{T=50 °C} –792 _{T=1000 °C}	794 _{T=50 °C} –1278 _{T=500 °C} 600 _{T=327 °C} 790 _{T=727 °C} 630 _{T=501 °C}	Rimax [28] for 89% T.D. [64] for 87% T.D. [65]
Zirconium oxide	469 _{T=50 °C} –651 _{T=1000 °C}	400–550 _{T=30–1000 °C}	for partially stabilized [63]
LBE	–	148 _{T=130 °C} –136 _{T=820 °C} ^{c)}	– [12]

^{a)}Including phase transition; ^{b)}RT: room temperature; ^{c)}Calculated with the following equation $c_{p,LBE}/(J\ kg^{-1}\ K^{-1}) = 164.8 - 3.94 \times 10^{-2} \cdot T/K + 1.25 \times 10^{-5} \cdot (T/K)^2 - 4.56 \times 10^5 \cdot (T/K)^{-2}$ for $T = 127\text{--}827\ ^\circ\text{C}$.^[12]

The glass transition temperature limits the use of the materials as filler material. Therefore, the glasses should not be used at temperatures above 540 °C, respectively 550 °C. The ceramics can be used up to at least 1000 °C, since no glass transformation was observed during DSC measurements.

However, the maximum long-term temperature resistance for all materials should be further investigated before being used in a long-duration thermal storage.

3.2.3. Thermal Conductivity (λ)

The data from the literature for similar materials to the potential filler materials investigated can be found in Table 3.

When considering the thermal conductivity of the materials, one can note the high thermal conductivity and the spread of

values for aluminum oxide (90%). In the case of the material with 90% aluminum oxide given in the literature, the composition of the remaining 10% is unknown. Since the composition of the 10% of other oxides has a very strong influence on the microstructure, which, in turn, can lead to a strongly altered thermal conductivity, an exact determination of the thermal conductivity is essential for final evaluation of thermal conductivity.

Furthermore, a relatively high thermal conductivity of 14.3 W m⁻¹ K⁻¹ is reported for zirconium silicate with 100% theoretical density,^[27] whereas porous materials have a significantly lower thermal conductivity. The material studied in this work consists of grains and a surrounding glassy phase, which has a similar composition to the grains (see Table 10). The values given by the manufacturer of the Rimax beads^[28] are in the same range as those found in the literature.

Table 3. Thermal conductivity data of the potential filler materials based on literature data for similar materials are given, as well as the thermal conductivity of LBE for comparison.

Material	$\lambda_{supplier}$ [W m ⁻¹ K ⁻¹]	$\lambda_{literature}$ [W m ⁻¹ K ⁻¹]	References
Diamond Pearls	n.a.	n.a.	–
Borosilicate glass	n.a.	1.2 _{T=90 °C}	[26]
Al ₂ O ₃ (90%)	n.a.	15–20 _{RT} ^{a)} 14–24 _{T=30–100 °C}	for 86–94.5% Al ₂ O ₃ [45] for 86–95% Al ₂ O ₃ [63]
Steatite	3 [55]	2–3 _{T=30–100 °C}	[63]
Zirconium silicate (Rimax)	7.7 _{T=250 °C} Rimax [28]	5.381 _{T=327 °C} 4.204 _{T=727 °C} 14.3 _{T=24.85 °C} 4.2 _{T=727 °C}	for 89% T.D. ^{b)} [64] for 100% T.D. ^{b)} [27] for 87% T.D. ^{b)} [65]
Zirconium oxide	n.a.	2–3 _{T=100 °C} 2 _{T=100 °C}	for PSZ [66] for tetragonal zirconia polycrystal (TZP) [66]
LBE	n.a.	11.1 _{T=250 °C} ^{c)} 14.4 _{T=500 °C} ^{c)}	[12]

^{a)}RT: room temperature; ^{b)}T.D.: theoretical density; ^{c)}Calculated with the following equation $\lambda_{LBE}/(W\ m^{-1}\ K^{-1}) = 3.284 + 1.617 \times 10^{-2} \cdot T/K - 2.305 \times 10^{-6} \cdot (T/K)^2$.^[12]

Overall, borosilicate glass, steatite, zirconium silicate, and zirconium are suitable for their use in a packed-bed TES with a liquid metal as the HTF due to their thermal conductivity.

4. Static Corrosion Tests

In the following, first, the methodology of the material compatibility test of the potential filler material in stagnant LBE as well as the general corrosion mechanism of ceramics and glasses in liquid metals are presented in Section 4.1. Second, the results of the static corrosion tests of the materials are discussed one by one in Section 4.2.

4.1. Methodology for Compatibility Testing

4.1.1. Corrosion Experiment in Stagnant LBE

The corrosion experiment in liquid LBE was conducted in the existing corrosion test facility CORrosion test stand for STagnant liquid Alloys (COSTA) at KIT.^[29] It consists of a furnace with a quartz tube as the reaction chamber, which can be purged with a defined gas. A gas mixture of 95% argon and 5% hydrogen (Ar5%H₂) with a volume flow of 100 mL min⁻¹ was used to reach a reducing atmosphere in the furnace. This atmosphere corresponds to a worst-case scenario, since, later on, in an operating plant, there will always be a small amount of oxygen to protect the piping, fittings, and other components of the plant from corrosion from LBE.^[12] An incident occurred during the 4 week tests that caused oxygen to enter the tube furnace for a brief time. As shown in **Figure 2**, there was a tantalum sheet in the LBE, where the spheres were stored. Since, according to the Ellingham diagram^[30] (specific data can be found in refs. [12,31]), tantalum has a higher affinity for oxygen than Pb or Bi and the sheet was not completely oxidized (tantalum oxide is white and porous), it can be assumed that the oxygen content in the LBE reached a maximum value of 1×10^{-17} wt% even during the oxygen incident.

The test temperature in the furnace was 500 ± 5 °C. The material samples were placed in liquid metal-filled Al₂O₃ crucibles (Giess- Technische- Sonderkeramik GmbH & Co. KG, quality AL99-G, (99.7% Al₂O₃)) that were located on a carrier for better loading and unloading. Each filler material sample was placed inside one crucible. The material samples float because the density of the potential filler materials is lower than that of the liquid heavy metal. A bent sheet made of tantalum was used to hold the samples below the liquid surface to ensure that the samples were always completely surrounded by the liquid, as shown in

Figure 2. Additionally, it was weighed down with small molybdenum cylinders.

The auxiliary materials used here, made of tantalum and molybdenum, are not expected to be soluble in or react with LBE at 500 °C under reducing conditions.^[32–34]

Before loading the sample, the LBE was conditioned in the COSTA facility at 500 °C in an Ar5%H₂ environment for 1 week. The glove box was evacuated several times and flushed by Ar5% H₂, until an oxygen partial pressure of 10^{-14} ppm was reached. The glove box was then connected to the quartz tube of the furnace to maintain the reducing atmosphere during loading and unloading the sample, as shown in **Figure 3**. The carrier with the LBE-filled crucible was transferred to the glove box so that the sample, the tantalum sheet, and the molybdenum cylinders could be placed in the Al₂O₃ crucibles. Tests with two different exposure times, 1 and 4 weeks, were performed. One carrier with samples was foreseen for each exposure time.

4.1.2. Sample Preparation for Energy-Dispersive X-ray Spectrometer Analysis after Exposure to LBE

After the exposure of the material samples, the adherent LBE on the samples surface was removed by a mixture of 1:1:1 of 30% hydrogen peroxide (Emsure, Merck KGaA), 96% acetic acid (Emsure, Merck KGaA), and absolute ethanol (VWR Chemicals BDH), as was described by Schroer.^[35] Huang et al.^[36] investigated the corrosiveness of a similar washing solution with 30% hydrogen peroxide, 40% acetic acid, and 30% ultrapure water instead of ethanol as a solvent on stainless steel. They found a relative mass loss of stainless steel for less than 0.5% for an exposure time of 144 h.^[37] It was shown for steel that the washing solution did not cause any additional, significant corrosion effects. Subsequently, the samples were washed with distilled water.

No data is available in the literature about the influence of the washing solution mentioned to remove the adhering LBE from the glass spheres. An exchange of Na⁺ ions of the glass by H⁺ ions of the aqueous solution is described in the literature.^[37,38] The as-delivered glass spheres (borosilicate glass spheres and Diamond Pearls) were stored in the solution with a pH value of about 2 for 24 h each, the maximum cleaning time of the sphere. The exposure test of the glass spheres is conducted to investigate whether there is any appreciable exchange of ions in the glass with those in the solution. Afterward, they were analyzed by a scanning electron microscope (SEM) and an energy-dispersive X-ray spectrometer (EDS).

The surface of the spheres showed no visible changes under SEM compared to the as-delivered spheres. Only a slightly lower

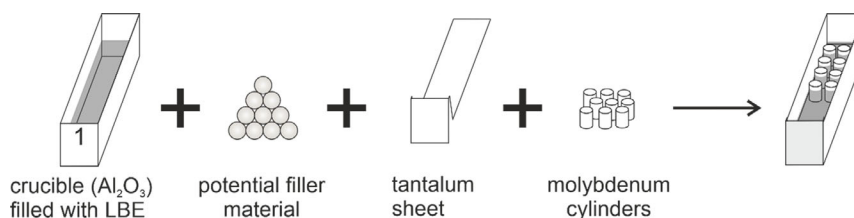


Figure 2. Sketch of the arrangement of the sample and the sinker (sheet and molybdenum cylinders) in the LBE-filled Al₂O₃ crucible.

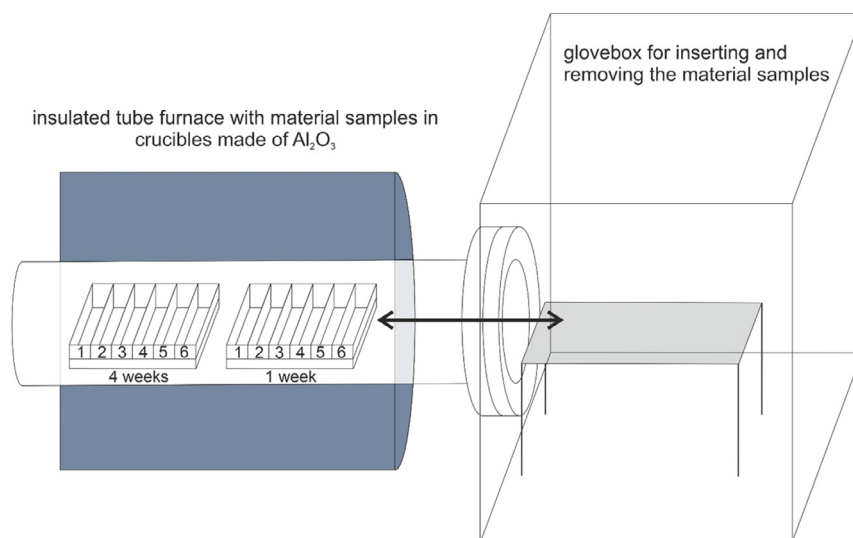


Figure 3. Schematic of the corrosion test stand. Left: Insulated tube furnace with the quartz tube in which the LBE-filled crucibles on carriers are located. Right: Glove box, with a small bench on which the carriers can be pulled and material samples can be added or removed.

sodium share could be observed for the Diamond Pearl. However, the sodium content also varies from sphere to sphere. The other components measured by EDS do not vary significantly.

The sodium content of the borosilicate glass spheres was measured to be 18% lower on average after exposure to the wash solution determined using EDS, but it is also well within the standard deviation (see Table 5). The silicon content of the sample exposed to the wash solution is slightly higher. This is probably due to small variations between the different spheres.

It is somewhat difficult to draw conclusions regarding the sodium content of the different spheres (as-delivered, after exposure to LBE for 1 and 4 weeks), since their composition differs slightly from sphere to sphere. However, the sodium content at the surface of a sphere compares well, even if the sphere was to interact with the washing solution. The influence of the washing solution should be the same for the entire surface of a sphere, since the entire surface of this sphere was exposed to the same washing solution under the same conditions.

4.1.3. Analysis of the Material Samples by SEM and EDS

All samples were analyzed using SEM with an EDS. The samples examined were previously sputter coated with gold, and a silver paste was used to ensure the conductivity of the sample to the sample holder. The SEM images were taken at an accelerating voltage of 15 kV and magnification between 30 and 15 000 \times . The EDS measurements were performed on several image sections of the sample, with about 10–30 measurement points taken per image. The measurement time of a single measurement point was at least 20 s, since a longer measurement time did not change the result significantly. Cross sections were prepared and examined from samples with a more severe corrosion attack.

The following aspects need to be taken into consideration when interpreting the EDS spectra. The electron beam has a certain penetration depth depending on the density of the material

investigated and the electron beam acceleration. It is in the range of 1–3 μm for the materials investigated here.^[39] Moreover, the beam has a certain extension; thus, the material around the point of interest is also measured when trying to determine the composition of very small particles. The material composition of the spheres is often inhomogeneous; therefore, the composition given should be seen more as an indication. Furthermore, elements with an atomic number lower than 11 cannot be quantitatively determined reliably.^[40] The elements in the EDS spectrum are always indicated proportionally, which is why it is especially useful to compare the ratio of different elements before and after the exposure to LBE at 500 °C. It was always measured at the surface at the top of the spheres to keep the error small due to the nonplanar surface.

4.1.4. General Corrosion Mechanism and Corrosion Parameters

The Ellingham diagram is used to estimate whether oxidation or a reduction of an element or oxide occurs at a given temperature in the presence of oxygen at a given partial oxygen pressure or in the presence of other elements, respectively, oxides.^[30] However, the data are given only for pure substances and not for compounds of substances. The oxidation reaction of oxides (K_2O , SiO_2 , ZrO_2 , Al_2O_3 , MgO , and CaO) contained in the glasses and ceramics has a significantly lower free enthalpy than lead and bismuth; therefore, from a thermodynamic point of view, no reduction reaction of the ceramic or glass components should take place.

Another important corrosion mechanism is the solubility of individual elements or compounds in liquid metal. There is only little literature available of solubility of different elements or compounds in lead, bismuth, or the eutectic mixture of lead–bismuth.

Gumiński^[41] published data on the solubility of different elements in lead and bismuth at about 600 °C; a selection of these data is shown in **Figure 4**.

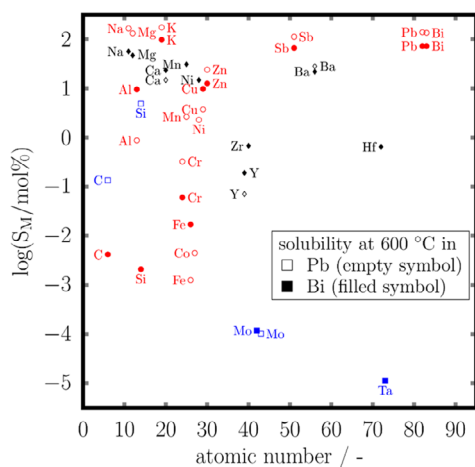


Figure 4. The logarithm of the solubility of different elements for elements with different atomic numbers in Pb (empty symbols) and Bi (filled symbols) is shown. Data are extracted from plots in ref. [41].

The data show the solubility of elements of the materials studied and, in addition, of more common elements (typical steel alloy constituents), such as Fe, Cr, and Ni. The empty circles stand for the logarithm of solubility of an element in lead, and the filled circles for the logarithm of solubility of an element in bismuth. The different symbols give more information on the determination of the values: the red circles correspond to a system of pure metal or a solid solution, where the solid solution is in an equilibrium. The black diamonds stand for a system where the saturated solution is in an equilibrium with an intermetallic compound consisting of the solute and the solvent. The blue squares show data for the solubility for which only the detection limit could be specified. The lowest solubility was generally found for Nb, Ta, Mo, W, and Re. It should be kept in mind that trace elements in the solute or solvent often influence the experimentally determined solubility. Furthermore, low solubility (<0.1 mol%) has a particularly high uncertainty. Some of the data points are determined by the apparent solubility from oxides, nitrides, or carbides instead of the pure metals, and the solubility of the pure metal is then calculated. Since there is no established method, as Gumiński notes, the data should be treated with critical eyes. The data points for the elements of Be, V, U and Si were calculated by Gumiński with the semiempirical model from Yatsenko.^[42]

Figure 4 shows a very high solubility of aluminum especially in lead, but also in bismuth. In the literature, aluminum oxide with high purity is described as very stable in LBE.^[43,44] The oxides of Al, Mg, and CaO-stabilized zircon and zirconia (all produced by the hot pressing process) also show good corrosion resistance against LBE,^[44] whereas the pure elements show decent solubility in LBE.^[41] Cook^[43] describes good corrosion resistance of MgO, Al₂O₃ as a single crystal, and CaO-stabilized ZrO₂ in lead.

However, little is known about the behavior of less-pure oxides and glasses or glassy structures in LBE. Industrial-grade alumina (80–99% Al₂O₃), for example, shows decreasing thermal conductivity with decreasing Al₂O₃ content,^[45] and is also less expensive

than pure Al₂O₃, which makes this material even more interesting for application as a potential storage material.

Structural ceramics are composite materials of structure-forming grains and a glassy phase which contain a higher share of additives.^[46] The chemical composition of the glassy phase, which acts as a binder, is responsible for the chemical resistance of the ceramic to the liquid phase with which it is in contact. The corrosion resistance of aluminum oxide in aqueous solutions decreases as the binder phase increases.^[46] Such a correlation is also plausible for ceramics in contact with LBE when the binder phase is attacked.

The intergranular corrosion of Al₂O₃ ceramics is reported to occur in liquid phase sintered materials in particular, since there is a glassy phase present, which is more accessible to corrosion, whereas almost no corrosion is observed in solid-phase-sintered or hot-pressed materials. However, it is not clear with which fluid the ceramics were in contact.^[47]

Gangler^[44] tested fused quartz for corrosion by LBE and found no corrosion attack. Asher et al.^[48] used a quartz glass apparatus for their lead (99.99% pure) loop, which operated up to 1000 °C under a reducing atmosphere. They described a failure of the quartz glass when oxygen entered their system and assumed an interaction of lead oxide with the silica.

Bach et al.^[49] heated pure silica glass with a layer of PbO and observed a new layer formation, whereas they found penetration of Pb²⁺ in glasses with Na₂O as an additive.^[49] The authors hypothesize that the glasses with Na₂O have a more fractured Si–O–Si network and, thus, the Pb²⁺ ions can penetrate better during thermal treatment compared to pure silicate glass.^[49]

4.2. Results of the Static Corrosion Tests

In the following, SEM images of the spheres before and after exposure to LBE are shown. The spheres exposed were cleaned from adherent LBE, as described in Section 4.1.2. The measuring points of the EDS measurement were categorized according to optical criteria of the SEM images and evaluated by assigning possible deviations of the composition to optical surface anomalies.

The solubility shown in Figure 4 is used for selecting the reference element. Furthermore, only reference elements with a total share in the material of more than 2 at% were investigated, since EDS data for <2 at% are not reliable to describe the share of the element in the composition of the material investigated based on previous experience.

4.2.1. Sodium Glass: Diamond Pearls

The Diamond Pearls are glass beads that are chemically and mechanically treated, polished, and hardened.^[50] Concerning the information from the supplier (Mühlmeier GmbH & Co.KG), they consist of: 61–67 wt% SiO₂, 10–18 wt% Na₂O, 5–10 wt% CaO, 3–8 wt% Al₂O₃, 1–5 wt% B₂O₃, and 0.5–3 wt% MgO.^[50] An additional inductively coupled plasma–optical emission spectrometry (ICP–OES) and carrier gas hot extraction, determined by the Institute for Applied Materials, Applied Materials Physics, chemical analysis (KIT), showed the following results: 44.5 wt%

O, 27.4 wt% Si, 11.9 wt% Na, 4.0 wt% Ca, 1.8 wt% Al, 0.9 wt% B, 2.1 wt% Mg, 1.6 wt% Zn, 0.4 wt% Sb, and 0.03 wt% Zr.

The SEM images of the as-delivered material are depicted in **Figure 5**. The surface is smooth, and shows only slight imperfections, such as indentations at the surface and some very small adherence from the same material. The chemical composition in atomic percentage measured by EDS and the values of the composition related to Si are depicted in **Table 4**. Since Si shows the lowest solubility in Bi and the second lowest in Pb, Si was chosen as the reference element. No significant compositional differences within one sample were found by EDS overall, but the composition varied slightly from sphere to sphere. Only measurements from the surface and not from pits, as can be seen in **Figure 5b,c**, were considered for the evaluation of the composition to avoid additional errors.

The element shares of Si and Na determined by EDS agree very well with the ICP–OES measurements. The small shares of the elements Ca, Mg, and Al determined by EDS, which are more error prone, are somewhat larger than those determined by ICP–OES. Additionally, not all elements were determined by EDS, such as B, Zn, Sb, and Zr, which leads to an

additional deviation of the shares comparing the two different methods presented here.

The surface of the Diamond Pearls exposed for one week to LBE is shown in **Figure 6**. The surface can be distinguished into two main areas, a brighter and a darker one, as shown in **Figure 6a,b**. The EDS measurements of the brighter surface show an increased lead and bismuth content up to 7.5 at% Pb and about 27 at% Bi, indicating an interaction of the glass with LBE. The Bi content is higher than the Pb content, which is in contrast to the higher solubility of Si in Pb shown in **Figure 4**. The bright areas occur both as spots and as patches, see **Figure 6c**. The deposits appear all over the sphere, but do not completely cover it.

Cracks visible in **Figure 6a** are probably a result of the thermal shock when the sphere was put in the Al₂O₃ crucible filled with hot LBE.

Figure 7 shows images of the surface of the Diamond Pearls after being exposed to LBE for 4 weeks.

In contrast to the spheres exposed for 1 week to LBE, bright areas can no longer be observed on the surface, but the latter is partially fissured and chipped off in layers (**Figure 7b**).

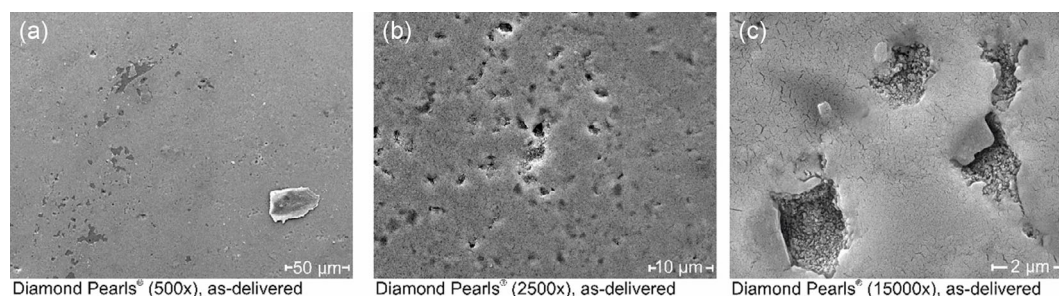


Figure 5. SEM images of the surface of the Diamond Pearls as-delivered.

Table 4. Composition of Diamond Pearls determined with EDS. All data of the shares are given in at% or the ratio of the shares ((at%) (at%)⁻¹).

		Na	Mg	Ca	Al	Si	Pb	Bi	Na/Si	Mg/Si	Ca/Si	Al/Si
As-delivered	Total	11.8	6.0	5.0	2.7	20.5	–	–	0.6	0.3	0.2	0.1
		± 0.7	± 1.6	± 0.9	± 0.5	± 2.1			± 0.1	± 0.1	± 0.0	± 0.0
Washed with solution (4.1.1)	Total	8.2 ± 0.9	2.3	3.2	2.1	27.0	–	–	0.3	0.1	0.1	0.1
			± 0.2	± 0.5	± 0.4	± 3.2			± 0.1	± 0.0	± 0.0	± 0.0
One week in LBE	Surface	11.6	4.5	3.3	2.6	19.5	0.2	0.2	0.6	0.2	0.2	0.1
		± 0.7	± 0.5	± 1.4	± 0.5	± 4.6	± 0.1	± 0.1	± 0.1	± 0.0	± 0.0	± 0.0
	Bright surface	9.7 ± 2.2	5.2	3.8	3.4	14.0	1.2	4.5	0.8	0.5	0.3	0.3
			± 1.1	± 1.4	± 1.2	± 6.5	± 1.2	± 6.5	± 0.2	± 0.3	± 0.1	± 0.2
Four weeks in LBE	Surface	8.3 ± 1.1	5.6	4.9	3.9	26.1	3.0	0.8	0.3	0.2	0.2	0.2
			± 0.6	± 1.8	± 0.6	± 6.4	± 0.9	± 0.3	± 0.1	± 0.0	± 0.0	± 0.0
	Fissured surface	4.6 ± 1.4	1.5	0.9	1.7	28.5	0.6	0.3	0.2	0.1	0.0	0.1
			± 0.3	± 0.6	± 0.5	± 9.8	± 0.7	± 0.2	± 0.1	± 0.0	± 0.0	± 0.0
	Revealed Smooth surface	9.5 ± 2.4	3.0	2.2	3.0	27.5	0.8	0.4	0.4	0.1	0.1	0.1
			± 0.6	± 1.2	± 0.5	± 7.5	± 0.2	± 0.1	± 0.2	± 0.0	± 0.0	± 0.0

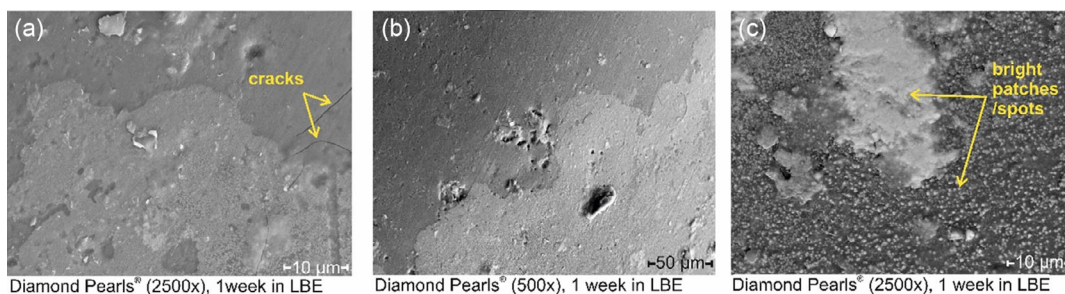


Figure 6. SEM images of the surface of the Diamond Pearls after exposure to LBE for 1 week at 500 °C.

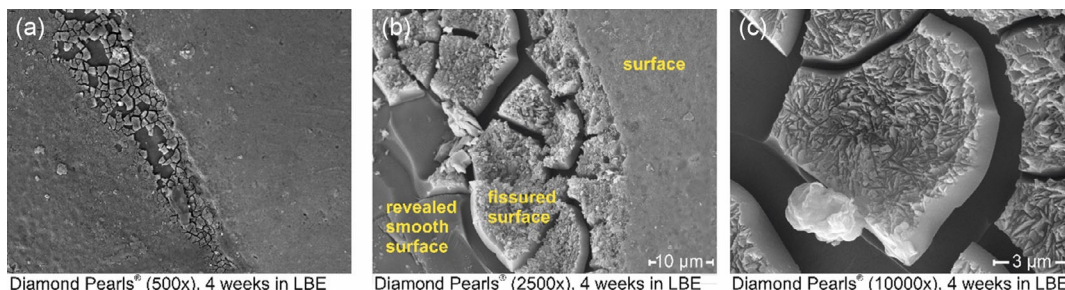


Figure 7. SEM images of the surface of the Diamond Pearls after exposure to LBE for 4 weeks at 500 °C.

Beneath the chipped surface, a smooth surface appears, which partly shows cracks again.

Figure 7c shows a devitrification with platelet-shaped crystals of the chipped surface.

When comparing the EDS spectra of the three representative structures, “surface”, “fissured surface”, and “revealed smooth surface”, shown in Figure 7b, the Na/Si, Mg/Si, Al/Si, and Ca/Si ratio in the fissured surface is significantly lower than in the surface or the smooth surface revealed. The lead content in the fissured surface is lower than in the “surface”, where the lead content is about 3 at% with a scatter of 0.9 at%. However, the composition even in the “surface” differs slightly from the as-delivered sphere; the variation in the composition of the spheres and a potential influence by the washing solution must also be taken into account. The mean lead content in the flakes themselves and also in the surface below the flakes is less than 1 at%. The bismuth content is also slightly increased in all three surface structures described. The atomic shares measured determined by EDS and the corresponding standard deviations are given in Table 4.

The elements Na, Mg, Ca, and Al show a very high solubility in both Pb and Bi (see Figure 4). Therefore, it seems plausible that these components are leached by the liquid metal in the fissured surface area. Selective dissolution of the elements from the glass network could then lead to the instability of the network, which, in turn, leads to a devitrification and chipping of the top layer. The underlying surface, again, has a slightly higher share of the elements mentioned compared to the fissured surface, but a lower share than in the surface. Parts of the surface are more affected by corrosion than others.

The flaking off and formation of cracks which were already visible on the surface after 1 week make this material unsuitable as a filler material in a packed-bed TES.

4.2.2. Borosilicate Glass

The borosilicate glass spheres investigated were supplied by Schäfer Glas GmbH. The composition of the spheres made of Schott Duran is given as: 81 wt% SiO₂, 13 wt% B₂O₃, 4 wt% Na₂O + K₂O, and 2 wt% Al₂O₃.^[26]

The surface of the as-delivered sample is smooth but has a high number of small indentations, as shown in Figure 8. Table 5 shows the composition of the as-delivered borosilicate glass spheres, however, without the boron fraction, since this is highly error prone in the EDS measurement due to the low atomic weight. As before, Si was used as the reference element for the EDS evaluation.

After 1 week, corrosion of the surface occurred and is depicted in Figure 9. Regarding the Diamond Pearls, there are again bright and dark areas on the surface, see Figure 9a,b, in which there is a dark area (1), presumably not wetted or time-delayed wetted with LBE, and a brighter (2) surface interspersed with craters. In Figure 9c, there are small white spots similar to the Diamond Pearls. As for the Diamond Pearls, the lead content is increased more in these areas than on the rest of the sphere. Furthermore, round dark spots can be seen in Figure 9c. The EDS measurements showed no significant difference from the other surface.

The EDS measurements did not generally show large differences in composition for the sphere exposed to LBE, thus, the averaged values over all measurements are given in Table 5.

A borosilicate glass sphere after 4 weeks exposed to LBE at 500 °C is shown in Figure 10.

Many very small, circular pits, almost all in the larger round areas, are visible after 4 weeks in LBE, in addition to the larger round areas, as shown in Figure 10a,b. Such circular pits are

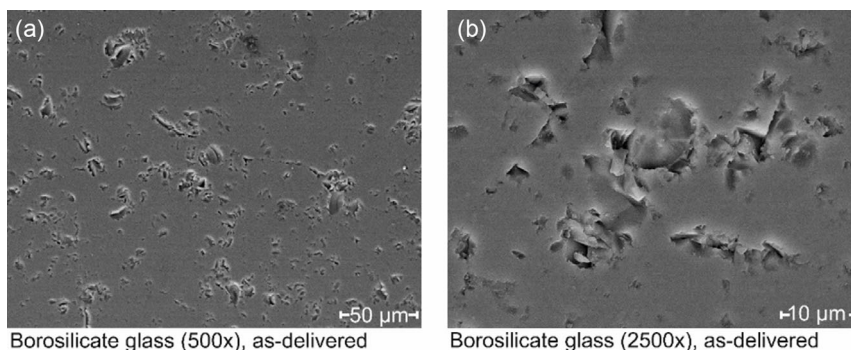


Figure 8. SEM images of the surface of the as-delivered borosilicate glass sphere.

Table 5. Composition of borosilicate glass sphere without the boron fraction measured by EDS. All data of the shares are given in at% or the ratio of the shares ((at%) (at%)⁻¹).

		Na	Al	Si	Pb	Bi	Na/Si	Al/Si	Pb/Si
As-delivered	Total	3.2 ± 0.5	1.9 ± 0.3	25.5 ± 2.8	–	–	0.1 ± 0.0	0.1 ± 0.0	–
Washed with solution	Total	2.7 ± 0.2	1.9 ± 0.1	36.2 ± 2.3	–	–	0.1 ± 0.0	0.1 ± 0.0	–
One week in LBE	Total	2.3 ± 1.1	1.4 ± 0.5	28.0 ± 10.3	6.3 ± 4.5	0.9 ± 2.2	0.1 ± 0.1	0.1 ± 0.0	0.3 ± 0.2
Four weeks in LBE	Surface	3.7 ± 0.6	1.5 ± 0.1	20.3 ± 2.0	5.3 ± 0.7	0.6 ± 0.1	0.2 ± 0.0	n.a.	0.3 ± 0.0
	Surface (dark areas)	2.2 ± 0.5	1.6 ± 1.9	22.9 ± 2.4	2.4 ± 0.6	0.3 ± 0.1	0.1 ± 0.0	n.a.	0.1 ± 0.0
	Fissured surface	1.2 ± 0.7	1.4 ± 0.2	25.2 ± 6.3	2.7 ± 1.8	0.4 ± 0.2	n.a.	n.a.	0.1 ± 0.1
	Fissured surface (bright areas)	3.5 ± 0.9	1.4 ± 0.1	18.0 ± 1.2	4.7 ± 0.8	0.6 ± 0.1	0.2 ± 0.1	n.a.	0.3 ± 0.1

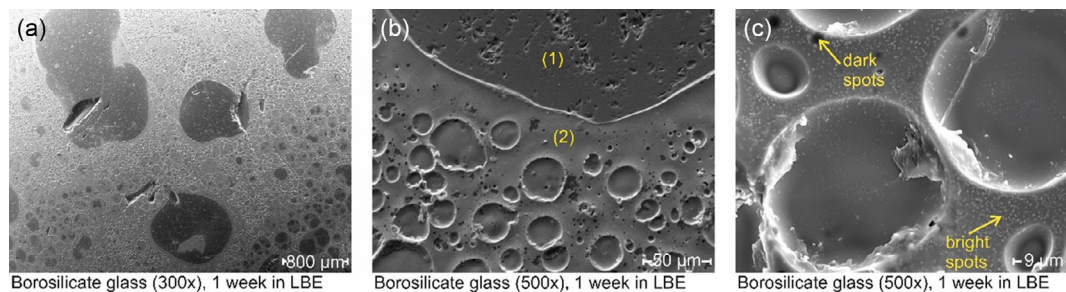


Figure 9. SEM images of the surface of the borosilicate glass sphere after exposure to LBE for 1 week at 500 °C.

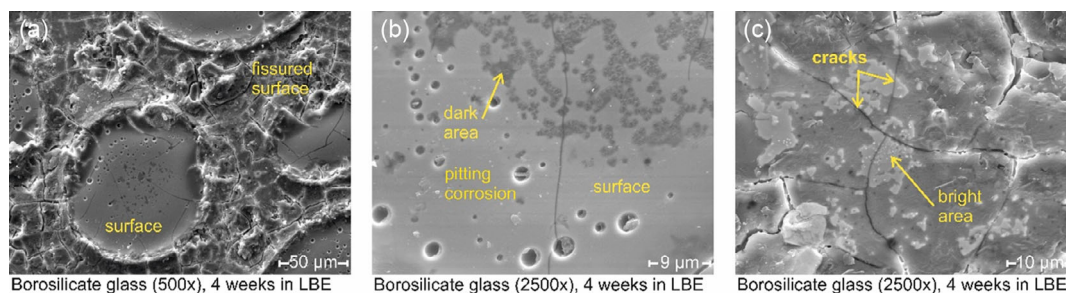


Figure 10. SEM images of the surface of the borosilicate glass sphere after exposure to LBE for 4 weeks.

observed and described for other materials combined with other fluids, for example, for metals or Zr–Ti–Cu–Al–Ni metallic glass.^[51] These observations are explained by pitting corrosion.

The spheres exposed to LBE exhibit a reaction mainly with Pb and scarcely with Bi. There are areas where the lead interacts more with the sphere: compare Table 5 “surface” and bright areas of the fissured surface. The dark areas in the SEM picture (Figure 10b) have a slightly lower lead content than the surrounding brighter surface. The bismuth content is also slightly increased, but the values are generally below 2 at%.

In Figure 10a,c, the surface between the crater-like surfaces shows cracks, which were not detected for the sphere exposed to LBE after 1 week. It is suspected that the elements contained in the glass are being dissolved out here or lead accumulated in the surface. The sodium content is lower in the fissured surface, except for the brighter areas, where the silicon content is decreased and the lead content is increased compared to the as-delivered sphere.

There are several possibilities for the causes of the pit formation, such as local lattice defects or solubility of a particular element. However, no element can be identified by EDS which is selectively dissolved out.

Compared to the Diamond Pearls, the borosilicate glass contains a significantly lower sodium content. By means of EDS, in contrast to the Diamond Pearl, no significant change in the overall sodium content can be detected after the borosilicate glass spheres have been exposed to LBE.

The appearance of the corroded surface of the Diamond Pearl and the borosilicate sphere differs. It is possible that, in addition to the composition and thermal history of the spheres, a different surface treatment also plays a role. However, similar to the Diamond Pearl, the corrosion appears after short exposure times and makes the material unsuitable for use as a filler material.

4.2.3. Aluminum Oxide (90%)

The datasheet of the aluminum oxide spheres (given by the supplier Mühlmeier GmbH & Co. KG) provides a material composition of the spheres of 90 wt% Al₂O₃, 4.5 wt% SiO₂, and 5 wt% alkaline metal oxides.^[52]

Very pure alumina is resistant to LBE^[44] and was, therefore, used as crucibles for the exposure tests in this study. Aluminum is used as reference element for the EDS evaluation, because the share of Si is too low and drops below 2 at% in the experiments

after exposure to LBE for 4 weeks and has the lowest solubility among the remaining elements measured by EDS.

In the literature, SiO₂, MgO, CaO, and Na₂O are reported, among others, as impurities but also as additives for alumina ceramics.^[53,54] The additives allow a lower sintering temperature by forming a vitreous phase and also a higher density of the sintered Al₂O₃ ceramic.^[53,54] However, the additional vitreous phase also results in decreased mechanical properties at high temperatures and a decreased corrosion resistance.^[53] Therefore, it is assumed that the additional elements accumulate mainly in the vitreous phase or the grain boundaries.

Figure 11 shows SEM images of the as-delivered Al₂O₃ spheres. In the case of the spheres investigated here, very different structures can be seen on the surface. On the one hand, the sphere has areas with a clearly visible vitreous phase (Figure 11b), and, on the other hand, there are areas on the sphere where the surface is strongly characterized by a crystalline appearance (Figure 11c). However, there are also areas where the two phases are not clearly separated and the crystal phase is partially covered by a vitreous phase.

The SEM images of the spheres after 1 and 4 weeks of exposure to LBE do not differ noticeably from the as-delivered sphere, shown in Figure 12. Since the vitreous phase is irregularly distributed at the as-delivered sphere, it is difficult to detect whether the vitreous phase decreased after exposure to LBE.

Only very small amounts of the additives Na, Mg, Si, and Ca were measured in the EDS analysis (Table 6). The shares of additives in the vitreous phase tend to be higher than in the crystal phase, as was also described by ref. [46]. Due to the strongly fluctuating values of the small shares, no conclusion can be drawn regarding whether the composition of the vitreous phase changes. It is expected that the glass phase is affected by LBE corrosion as it was observed for the glasses, since the glassy phase of the alumina contains the same elements as the glasses studied and the elements are also bound in a glassy structure.

The lead and bismuth contents measured after exposure to LBE are very low, <2 and 1 at%, respectively, after 4 weeks, but they tend to increase with exposure time. As expected, the lead and bismuth contents measured in the vitreous phase are more scattered and they are higher compared to the crystalline phase. It is expected that lead and bismuth can penetrate more easily into the glass phase because of a higher number of free network bonds than in the crystal phase, as it was supposed for the glass containing sodium.^[49] Further investigations are

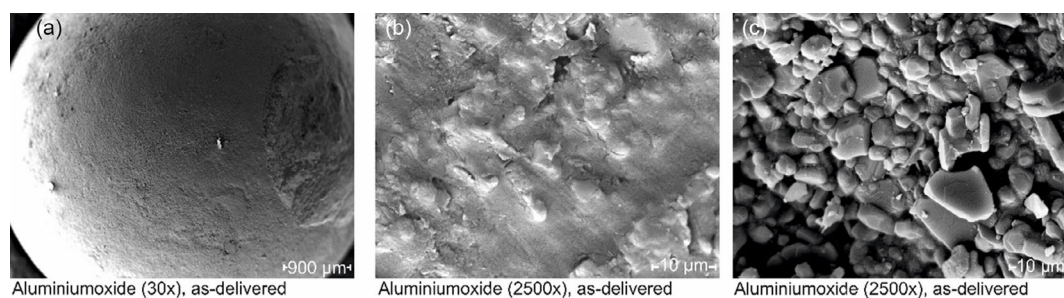


Figure 11. SEM pictures of the aluminum oxide (90%) sphere as-delivered. a) Magnification of 30×, b) vitreous phase, and c) crystal phase. All pictures were taken of the same sphere.

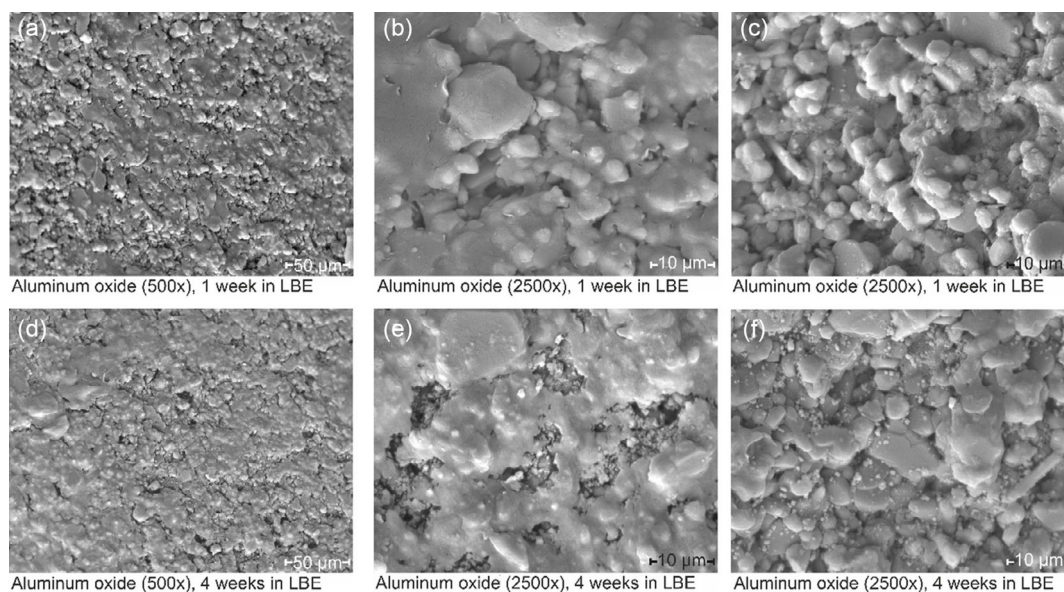


Figure 12. SEM pictures of the surface of aluminum oxide (90%) spheres after exposure to LBE for a–c) 1 week and d–f) 4 weeks.

Table 6. Composition of an aluminum oxide (90%) sphere measured by EDS. All data of the shares are given in at% or the ratio of the shares ((at%) (at%)⁻¹).

		Na	Mg	Al	Si	Ca	Pb	Bi	Mg/Al	Si/Al	Ca/Al
As-delivered	Vitreous phase	1.3 ± 1.5	3.1 ± 2.7	46.7 ± 10.3	4.7 ± 3.1	3.8 ± 5.1	–	–	0.1 ± 0.1	0.1 ± 0.3	0.1 ± 0.2
	Crystal phase	0.8 ± 0.6	1.1 ± 0.7	48.1 ± 10.6	2.7 ± 1.8	0.6 ± 0.9	–	–	0.0 ± 0.0	0.1 ± 0.1	0.0 ± 0.0
One week in LBE	Vitreous phase	1.8 ± 5.4	1.7 ± 2.1	46.0 ± 13.0	2.2 ± 1.5	0.6 ± 0.7	1.3 ± 3.8	0.2 ± 0.7	0.0 ± 0.1	0.1 ± 0.1	n.a.
	Crystal phase	0.5 ± 0.2	0.8 ± 1.4	43.9 ± 9.4	1.7 ± 2.2	0.2 ± 0.4	0.4 ± 0.5	0.1 ± 0.1	n.a.	0.0 ± 0.1	n.a.
	Particle covered phase	0.8 ± 0.7	6.0 ± 4.2	39.2 ± 9.2	1.7 ± 1.0	3.6 ± 8.0	0.4 ± 0.7	0.2 ± 0.2	n.a.	0.1 ± 0.0	n.a.
Four weeks in LBE	Vitreous phase	2.0 ± 4.5	2.3 ± 2.1	45.5 ± 12.1	1.9 ± 1.3	1.0 ± 1.9	1.8 ± 2.5	0.8 ± 1.4	0.1 ± 0.1	n.a.	n.a.
	Crystal phase	0.5 ± 0.2	0.7 ± 0.4	40.3 ± 5.6	0.8 ± 0.3	0.1 ± 0.1	0.5 ± 0.4	0.1 ± 0.2	n.a.	n.a.	n.a.

needed to determine the corrosion resistance of aluminum oxide (90%). In comparison to the glass spheres tested, the corrosion is very low and acceptable after these short exposure times.

4.2.4. Steatite

Steatite is a magnesium silicate ceramic. The composition of the material investigated is shown in **Table 7** and given by the supplier (CeramTec GmbH) according to DIN standard for C220 with a maximum of 64 wt% SiO₂, a maximum of 31 wt% MgO and 4 wt% Al₂O₃, 1.4 wt% Fe₂O₃, and 1.2 wt% Na₂O + K₂O.^[55] Steatite consists of a crystalline phase (70–80%) and an embedded glassy phase (20–30%) at room temperature,^[56] as shown in **Figure 13**, where the crystal structure appears brighter than the glassy phase (referred to as “glassy phase 1”). The composition of the small and bright particles on the surface is difficult to be determined by EDS due to their small size and is, therefore, strongly error prone, which is also reflected in the large standard deviation of the measurements. The particles seem to have a similar composition in the glassy and crystal phase.

The crystals consist mainly of protoenstatite (Mg₂Si₂O₆)^[57] embedded in Si-rich phase.^[58] The EDS analysis of the as-delivered sphere also showed a ratio of Mg to Si of about 1 (Table 7), which corresponds to the stoichiometric composition of the crystalline phase described. The vitreous phase, on the other hand, contains significantly more Si, as shown in Table 7.

After exposure to LBE for 1 week, the crystalline phase appears darker than the glassy phase (glassy phase 2) in some parts of the surface, as shown in **Figure 14a**. In other areas on the surface, it is just the opposite, and the glassy phase appears darker (glassy phase 1) than the crystalline phase, as it is the case for the as-delivered sphere.

The surface of the sphere exposed to LBE for 4 weeks looks similar to the one after 1 week (Figure 14b). Figure 14c shows a cross section of a steatite sphere exposed to LBE for 4 weeks. The crystalline structure can be clearly seen and is embedded into the vitreous phase, which appears brighter in the near-surface area of the sphere and vice versa in the more inner area.

Elements with a higher atomic number appear brighter in the SEM images.^[40] Since the glass phase partially appears brighter

Table 7. EDS analysis of the as-delivered steatite sphere and the sphere exposed for 1 and 4 weeks to LBE. All data of the shares are given in at% or the ratio of the shares ((at%) (at%)⁻¹).

		Na	Mg	Al	Si	Pb	Bi	Mg/Si	Al/Si	Pb/Si	Bi/Si
As-delivered	Glassy phase 1	0.2 ± 0.2	11.3 ± 4.4	2.8 ± 1.1	21.3 ± 4.0	–	–	0.6 ± 0.2	0.1 ± 0.1	–	–
	Crystal phase	0.2 ± 0.2	16.5 ± 2.4	1.2 ± 0.5	16.9 ± 2.7	–	–	1.0 ± 0.1	n.a.	–	–
One week in LBE	Glassy phase 1 (dark)	1.0 ± 0.7	13.0 ± 5.3	3.0 ± 1.2	21.9 ± 7.4	0.6 ± 1.9	1.2 ± 4.9	0.6 ± 0.3	0.2 ± 0.2	n.a.	n.a.
	Glassy phase 2 (bright)	1.1 ± 0.6	8.8 ± 4.4	3.1 ± 1.3	20.9 ± 6.7	5.2 ± 4.8	0.6 ± 0.7	0.5 ± 0.3	0.2 ± 0.1	0.6 ± 1.9	n.a.
	Crystal phase	0.8 ± 1.2	18.2 ± 2.3	1.5 ± 1.1	18.2 ± 3.9	0.3 ± 0.5	0.2 ± 0.6	1.0 ± 0.1	n.a.	n.a.	n.a.
Four weeks in LBE	Glassy phase 1	1.2 ± 0.6	17.4 ± 4.1	3.7 ± 1.7	31.6 ± 7.9	1.0 ± 0.6	1.2 ± 0.6	0.6 ± 0.2	0.1 ± 0.1	n.a.	n.a.
	Glassy phase 2	2.5 ± 2.5	10.6 ± 5.5	3.7 ± 1.9	29.1 ± 9.4	8.0 ± 5.4	2.5 ± 2.5	0.4 ± 0.3	0.2 ± 0.2	0.3 ± 0.2	0.1 ± 0.1
	Crystal phase	1.5 ± 1.6	19.5 ± 4.0	2.4 ± 1.3	26.3 ± 8.7	0.7 ± 0.6	1.5 ± 1.6	0.8 ± 0.2	0.1 ± 0.1	n.a.	n.a.

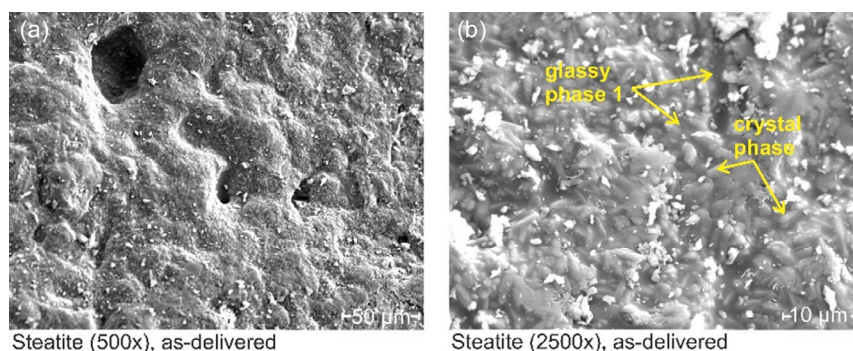


Figure 13. SEM pictures of the surface of an as-delivered steatite sphere. “Glassy phase 1” refers to the glassy phase which appears darker than the crystal phase.

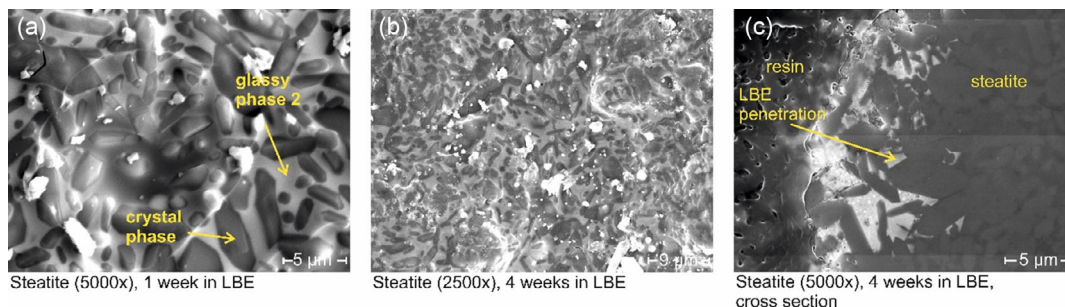


Figure 14. SEM image of the surface of the steatite sphere after exposure to LBE for 1 week a) and 4 weeks b). c) Cross section of a steatite sphere after 4 weeks of exposure with a penetration depth of LBE of about 10 µm. “Glassy phase 2” refers to the glass phase that appears lighter than the crystals.

than the crystal phase after exposure and removal of the LBE (Figure 14a), it can be assumed that Pb and/or Bi have penetrated there.

The EDS examinations confirm this finding, whereby significantly more lead than bismuth has penetrated into the glassy phase, as shown in Table 7. The lead content in the bright-appearing glassy phase is again significantly higher than in the dark-appearing glassy phase. The content in the crystal phase is very low.

It is assumed that the LBE does not completely wet the surface, which is the reason for a bright and dark-appearing glassy phase

existing in parallel after exposure to LBE. The predominant lead penetration into the glassy phase can be explained by the fact that all transport processes are slower than in disordered glassy phases in crystalline lattices. The Pb values determined vary very strongly, on the one hand, due to the penetration depth of the electron beam and, on the other hand, also due to an uneven LBE penetration into the sphere. The fact that a small amount of lead can still be measured in the crystal structure could also be related to the penetration depth of the electron beam into the sample. A lead-rich glass phase below the crystal phase at the surface could lead to the low lead content measured.

LBE penetrated the glassy phase here. It is known from other experiments that glass with lead inclusions tends to crack with thermocycling. Therefore, this material could not be considered as a filler material in a TES system.

4.2.5. Zirconium Oxide

The manufacturer (Final Advanced Materials GmbH) specifies the composition of zirconium oxide (zirconia) as 95 wt% of ZrO_2 and 5 wt% of Y_2O_3 .^[59]

The surface of zirconia appears smooth and uniform, with small dark dots visible on the surface, which are exemplarily circled in Figure 15a. The EDS measurements (Table 8) showed an increased Al content for the dark-appearing dots, which is plausible since some aluminum oxide is often added to zirconium oxide ceramics.^[60] Furthermore, the surface shows small indentations in some places and dark larger areas, as shown in Figure 15a. According to the EDS, these larger areas are probably carbon. However, carbon is difficult to detect with EDS because it has a low atomic number. The carbon on the surface could result from impurities from the environment, after the manufacturing process.

According to the EDS, the composition of the sphere seems to be homogeneous, except for the structures mentioned above.

The surface of the zirconium oxide does not show any detectable superficial changes after 1 and 4 weeks (Figure 16) of exposure to LBE.

No significant lead or bismuth content can be detected in the EDS analysis either. Small particles can be detected only in the indentations, which have a rough surface (Figure 16b cubical particles and Figure 16c platelet-shaped and rod-shaped particles). An analysis by EDS indicates an increased lead content. These are presumably lead-containing particles which may have been formed during cleaning with the solution described in Section 4.1.2 and which adhere there due to the rough surface in the indentation.

As described in Section 4.1.4, the corrosion of CaO-stabilized zirconia ceramics in LBE^[44] and Pb^[43] has been investigated in the literature and a very good corrosion resistance was reported. The Y_2O_3 -stabilized zirconia ceramic investigated also shows a very good corrosion resistance to LBE, similar to the CaO-stabilized zirconia ceramics described in the literature. Therefore, zirconia ceramics are promising candidates for filler materials in TES.

4.2.6. Zirconium Silicate

The main components of the zirconium silicate ceramic are ZrO_2 and SiO_4 . Depending on the ratio of the two components, $ZrSiO_4$, a tetragonal crystal structure, is formed, also called zircon. Additionally, a SiO_4 - or ZrO_2 -rich phase or a pure phase of one of these two components is present.^[61] Moreover, most of the zirconium silicate ceramics contain impurities and other

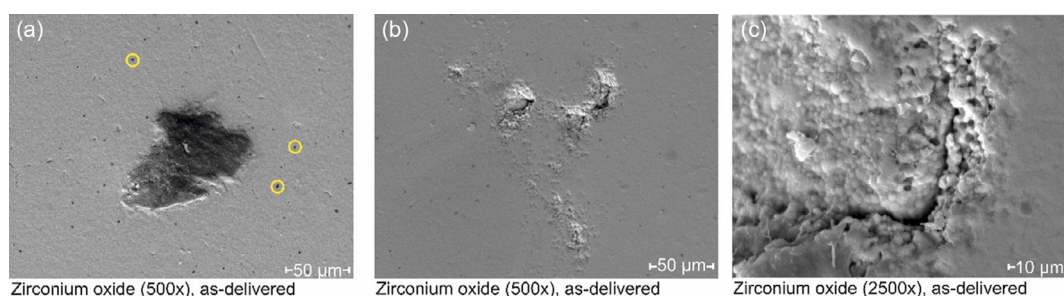


Figure 15. SEM pictures of the surface of the as-delivered zirconium oxide.

Table 8. EDS analysis of the as-delivered zirconium oxide sphere and the sphere exposed for 1 and 4 weeks to LBE. All data of the shares are given in at% or the ratio of the shares ((at%) (at%)⁻¹).

		Al	Y	Zr	Pb	Bi	Al/Zr	Y/Zr	Pb/Zr
As-delivered	Surface (bright, without dark spots)	4.1 ± 7.2	3.6 ± 1.3	37.1 ± 11.2	–	–	0.2 ± 0.5	0.1 ± 0.0	–
	Deposit at surface	5.5 ± 5.4	3.6 ± 1.7	36.1 ± 16.3	–	–	0.1 ± 0.1	0.1 ± 0.0	–
	Dark dots at surface	31.5 ± 7.8	2.3 ± 1.4	21.8 ± 15.4	–	–	2.0 ± 1.1	0.1 ± 0.0	–
One week in LBE	Surface (bright, without dark spots)	1.5 ± 1.4	3.0 ± 1.5	42.8 ± 17.1	2.1 ± 4.3	0.6 ± 2.4	0.1 ± ± 0.1	0.1 ± 0.0	0.1 ± 0.2
	Deposit at surface	2.5 ± 1.9	3.3 ± 1.8	32.3 ± 17.2	4.8 ± 5.9	5.9 ± 13.6	0.1 ± 0.1	0.1 ± ± 0.0	0.2 ± 0.3
	Dark spots at surface	28.5 ± 16.0	2.4 ± 1.3	30.8 ± 15.4	1.6 ± 3.1	0.3 ± 0.2	1.2 ± 0.7	0.1 ± ± 0.0	0.0 ± 0.1
	Cubical particle	2.2 ± 1.1	2.1 ± 1.0	24.4 ± 12.3	5.9 ± 2.7	0.1 ± 0.3	0.1 ± 0.1	0.1 ± 0.0	0.3 ± 0.1
Four weeks in LBE	Surface (bright, without dark spots)	1.7 ± 0.8	2.2 ± 0.9	26.8 ± 7.9	0.9 ± 1.1	0.4 ± 0.2	0.1 ± 0.0	0.1 ± 0.0	n.a.
	Deposit at surface	2.3 ± 1.5	2.0 ± 1.1	21.4 ± 10.2	3.6 ± 3.7	2.1 ± 6.9	0.1 ± 0.1	0.1 ± 0.1	0.2 ± 0.3
	Dark spots at surface	26.0 ± 6.6	1.5 ± 0.4	16.3 ± 3.4	0.4 ± 0.3	0.3 ± 0.1	1.7 ± 0.5	0.1 ± 0.0	0.0 ± 0.0
	Particles	1.8 ± 0.6	2.1 ± 0.5	21.0 ± 2.4	1.5 ± 0.8	0.3 ± 0.2	0.1 ± 0.0	0.1 ± 0.0	n.a.

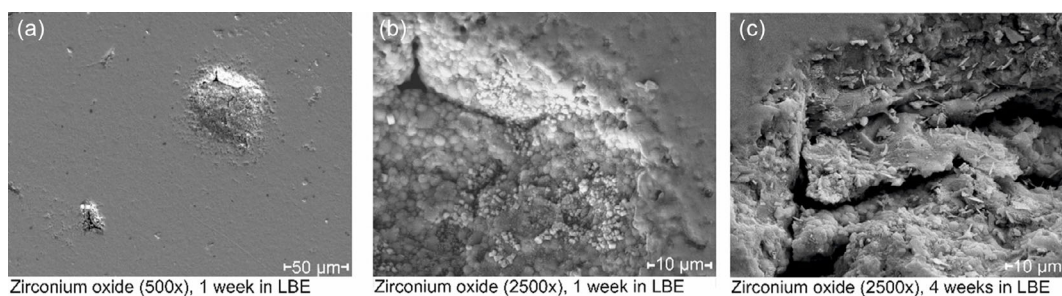


Figure 16. SEM pictures of zirconium oxide exposed to LBE for 1 a,b) and 4 weeks c).

elements. The manufacturer (Saint Gobain) of the ceramic beads investigated gives a composition of 58 wt% ZrO_2 , 37 wt% SiO_2 , and 5 wt% of other elements for the material (Rimax). The composition measured by EDS is given in **Table 9**. The ICP–OES and carrier gas hot extraction measurements carried out by the Institute for Applied Materials - Applied Materials Physics, chemical analysis (KIT), give a composition in wt% of the Rimax spheres of: 43.8 ± 1.2 Zr, 13.9 ± 0.6 Si, 1.21 ± 0.03 Al, 0.986 Hf, 0.338 ± 0.009 Ca, 0.242 ± 0.061 Y, and 35.5 ± 2.9 O. The ratio of the elements Si/Zr specified by the manufacturer (0.4) is in good agreement with the values determined from the ICP–OES measurement (0.29–0.34) taking into account its measurement uncertainty. The EDS measurements give the following ratio calculated from the weight percentages: 0.53 ± 0.16 at the surface. The ratios of Si/Zr determined by different methods are in good agreement taking the measurement uncertainties into account.

Figure 17a shows the surface of the Rimax bead and b) the surface of the bead after exposure in LBE for one and four weeks c).

The spheres in **Figure 17a,b** do not show any visible difference, and the compositions of the as-delivered spheres and

the spheres exposed to LBE for 1 and 4 weeks show no significant compositional differences in the EDS results (**Table 9**).

Only the aluminum content in the surface of the as-delivered sphere varies significantly, but is constant within a particular image section. Thus, an Al/Zr ratio of a minimum of 0.5 and maximum of 65 is measured in the as-delivered sphere, whereas the ratio of the sphere exposed to LBE for 1 week only varies from 0.3 to 2.7 and the sphere exposed to LBE for four weeks varies only from 0.3 to 4.2.

5. Zirconium Silicate as a Filler Material in a Lab-Scale TES

According to the results of the static corrosion experiments in stagnant LBE at 500 °C, both zirconium oxide and zirconium silicate are promising as filler materials. Since zirconium silicate is about half the price of zirconium oxide, it was used as a filler material in a lab-scale thermocline packed-bed storage configuration (VESPA, Vorversuch EnergieSpeicher Aufbau (ger.), engl. Preliminary test for energy storage setup) with LBE as the HTF. The TES was operated in a temperature range between 180 and

Table 9. EDS analysis of the as-delivered zirconium silicate sphere and the sphere exposed for 1 and 4 weeks to LBE. All data of the shares are given in at% or the ratio of the share ((at%) (at%)⁻¹).

		Al	Si	Zr	Pb	Bi	Al/Zr	Si/Zr	Pb/Si
As-delivered	Total	33.1 ± 24.3	13.2 ± 7.3	7.9 ± 4.6	–	–	12.7 ± 18.1	1.7 ± 0.5	–
One week in LBE	Total	13.9 ± 4.4	21.6 ± 6.3	16.5 ± 3.4	0.9 ± 1.3	0.4 ± 0.4	0.9 ± 0.4	1.3 ± 0.3	n.a.
Four weeks in LBE	Total	14.1 ± 6.7	15.2 ± 4.0	9.8 ± 2.9	1.8 ± 1.6	0.4 ± 0.5	1.6 ± 1.0	1.6 ± 0.2	n.a.

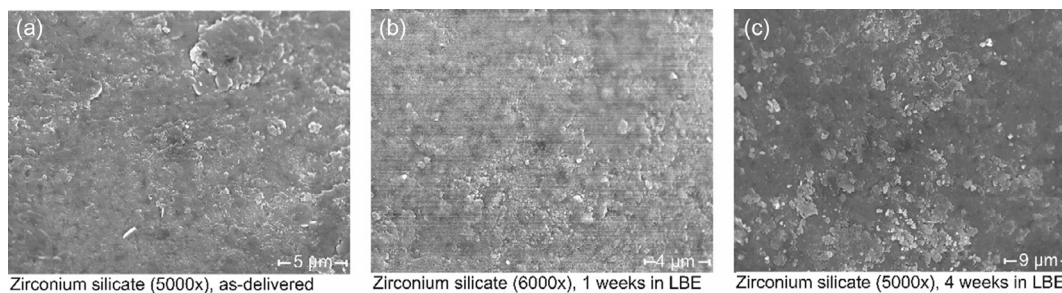


Figure 17. SEM picture of a Rimax grinding bead. a) Surface of as-delivered grinding bead, b) surface of grinding bead after exposure to LBE for one week, and c) surface of grinding bead after exposure to LBE for four weeks at 500 °C.

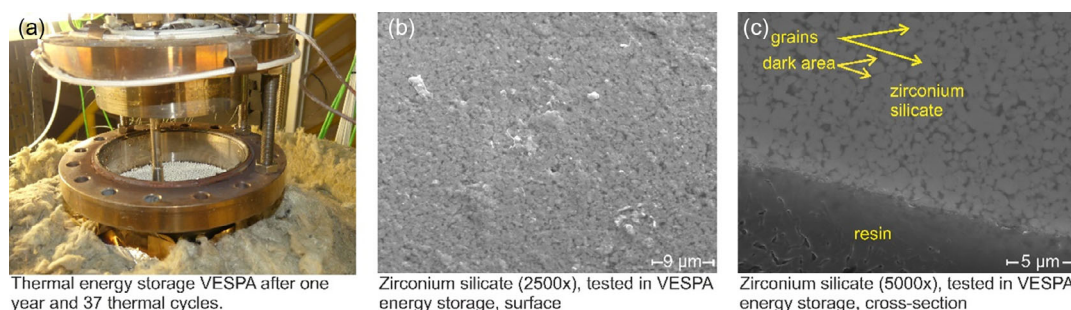


Figure 18. a) TES of the VESPA test facility after operation with the lid open, b) surface of Rimax bead after being tested in the VESPA experiment, and c) cross section of Rimax bead after being tested in the VESPA experiment.

380 °C. Within a year, 37 thermal cycles were realized; in the idle time, the TES temperature was at 180 °C. Further information on the experiments and the operational details are given in ref. [15].

The spheres in the storage did not show any changes visible to the naked eye before and after the experiments. After the experiments, the LBE did not adhere significantly and the beads could be removed easily. **Figure 18a** shows the TES of the VESPA facility after the experiments with the lid open.

An SEM image of the surface of the sphere and a micrograph of one of the beads (Rimax) used in the VESPA experiment in the storage tank are shown in **Figure 18b,c**.

The surface of the sphere has partially changed in terms of structure after the tests in the VESPA experiment. Most of the surface has a similar structure as the micrograph, where single grains are visible surrounded by a darker phase. However, there are still a few structures on the surface that resemble the ones on the surface of the as-delivered sphere.

No LBE penetration is visible to the naked eye in **Figure 18c**, which shows the polished section of the sphere used in the VESPA experiment. Confirming that, the EDS line profile measurement from the surface of the sphere into the core showed no increased Pb or Bi contents in the near-surface region.

Additionally, the grains of which the sphere is made, which are visible on the surface in the micrograph, were characterized by EDS and have the same composition within the standard deviation (**Table 10**).

However, the composition of the dark phase at the surface of the sphere differs from that inside the sphere. The aluminum fraction has a higher share in the EDS measurements on the surface but with a larger standard deviation. The Al/Zr fraction at the surface has decreased further compared to the sphere exposed to LBE for four weeks, but with a high standard deviation. In addition, the Si/Zr ratio of the dark area at the

surface is about 1.5 times higher than inside the sphere, see **Table 10**.

It is suspected that the as-delivered sphere shown in **Figure 17a** is surrounded by a glassy phase that is not completely stable to LBE. However, since no LBE has penetrated into the inner part of the sphere, zirconium silicate is still a promising material candidate.

Furthermore, zirconium silicate was successfully used as a filler material in the lab-scale TES at KIT. Further tests with more thermal cycles and at an elevated temperature (up to 750 °C) are planned.

6. Conclusion

The thermophysical properties of two glass and four ceramic materials, as well as their compatibility with LBE at 500 °C, were investigated in this article for use as potential filler materials for a packed-bed TES. The static corrosion experiments have shown that the glasses studied are unsuitable as storage materials for use with LBE as the HTF. In the case of the Diamond Pearls, there was surface corrosion and chipping of the surface. The surface of the borosilicate glass spheres showed corrosion and chipping of the surface as well. Furthermore, pitting corrosion is observed in the borosilicate glass. Particularly Na, Mg, and Ca seem to be leached out of the glass network in both glasses investigated.

Regarding the ceramics, steatite suffered from penetration by Pb particularly into the glassy phase and is, therefore, not suitable as filler material. The alumina (90%) has a large glassy phase, which could be attacked by the liquid metal. However, no reliable statement could be made by EDS about Na, Mg, and Ca in the glassy phase due to their low amount in the alumina ceramic and further investigations are necessary

Table 10. EDS analysis of the as-delivered zirconium silicate sphere and the sphere after use in a lab-scale TES (VESPA). All data of the shares are given in at% or the ratio of the shares ((at%) (at%)⁻¹).

		Al	Si	Zr	Pb	Bi	Al/Zr	Si/Zr	Pb/Si
As-delivered	Total	33.1 ± 24.3	13.2 ± 7.3	7.9 ± 4.6	–	–	12.7 ± 18.1	1.7 ± 0.5	–
Surface of the sphere used in VESPA experiment	Dark area	7.6 ± 5.3	22.9 ± 3.8	10.0 ± 2.1	0.0 ± 0.0	0.1 ± 0.0	0.9 ± 0.9	2.3 ± 0.4	n.a.
	Grains	1.5 ± 0.6	22.6 ± 2.9	15.9 ± 2.4	0.1 ± 0.1	0.1 ± 0.1	0.1 ± 0.0	1.4 ± 0.1	n.a.
Cross section of the sphere used in VESPA experiment	Dark area	1.9 ± 1.0	25.8 ± 4.2	17.0 ± 3.1	0.0 ± 0.0	0.1 ± 0.0	0.1 ± 0.1	1.5 ± 0.2	n.a.
	Grains	1.5 ± 0.5	20.0 ± 2.7	13.6 ± 2.0	0.0 ± 0.1	0.1 ± 0.0	0.1 ± 0.0	1.5 ± 0.1	n.a.

Zirconium oxide and zirconium silicate are two promising candidates according to the results of the static corrosion tests. Since the goal of the investigations presented here was to select a suitable filler material for application in a TES system and zirconium silicate was only half the price of zirconium oxide, the former was used for the lab-scale TES tests. No significant changes in the performance of the energy storage and the composition of the filler material could be detected after one year.

The following aspects were identified for further analysis: 1) Since the thermal storage systems will be operated at temperatures above 500 °C in the future, the ceramic materials will be exposed to liquid metal at higher temperatures (up to 750 °C) and longer exposure times; 2) There is a research gap in the literature regarding the corrosion of ceramics in liquid metals and their corresponding corrosion mechanisms. A better understanding of the corrosion mechanisms would simplify a selection of suitable ceramics and also of suitable process conditions during manufacturing; 3) There is some indication that the LBE wets the spheres incompletely. As the materials are to be used in a heat storage system, wetting is an important factor for the heat transfer between the fluid and the filler material and should, therefore, be investigated in more detail; and 4) Although the materials used here have been reported in the literature to have good thermal shock resistance and a low coefficient of thermal expansion, the thermal shock resistance and thermal fatigue resistance should still be investigated before the use of the materials in a TES.

Acknowledgements

The authors would like to thank Sabrina Herberger from the Institute of Thermal Process Engineering (TVT, KIT) for the determination of the density. The authors would also like to thank Stefan Sinning, Esther Heil, and all the students who contributed to this work.

Open access funding enabled and organized by Projekt DEAL.

Conflict of Interest

The authors declare no conflict of interest.

Data Availability Statement

The data that support the findings of this study are available from the corresponding author upon reasonable request.

Keywords

ceramics, corrosion, glasses, lead-bismuth eutectic, liquid metal, storage materials, thermal energy storage

Received: July 12, 2023

Revised: September 15, 2023

Published online:

- [1] M. v. d. Heyde, G. Schmitz, *Encyclopedia of Energy Storage*, Elsevier, Oxford **2022**, pp. 108–121.
[2] C. A. Schoeneberger, C. A. McMillan, P. Kurup, S. Akar, R. Margolis, E. Masanet, *Energy* **2020**, 206, 118083.

- [3] J. I. Burgaleta, S. Aria, D. Ramirez, in *Proc. 2011 SolarPACES*, Granada, Spain 20–23 September, **2011**.
[4] F. Dinter, D. M. Gonzalez, *Energy Procedia* **2014**, 49, 2472.
[5] G. J. Kolb, D. J. Alpert, C. W. Lopez, *Sol. Energy* **1991**, 47, 39.
[6] H. Kauko, A. Sevault, S. Vasta, H. Zondag, A. Beck, G. Drexler-Schmid, N. R. G. Polanco, Z. Ma, T. Roskilly, *EERA, Industrial Thermal Energy Storage - Supporting the Transition to Decarbonise Industry* **2022**, <https://d2m9e9.n3cdn1.secureserver.net/wp-content/uploads/2022/12/DU-WP-Ind-tes-web.pdf>.
[7] W.-D. Steinmann, *Thermal Energy Storage for Medium and High Temperatures-Concepts and Applications*, Springer Fachmedien Wiesbaden, Wiesbaden **2022**.
[8] C. K. Ho, *Sol. Energy* **2017**, 152, 38.
[9] J.-S. Kim, A. Dawson, R. Wilson, K. Venkatesan, W. Stein, in *Proc. ASME 2015 9th Int. Conf. on Energy Sustainability Collocated with the ASME 2015 Power Conf., the ASME 2015 13th Int. Conf. on Fuel Cell Science, Engineering and Technology, and the ASME 2015 Nuclear Forum*, 1, San Diego, CA June 28–July 2, **2015**.
[10] A. Palacios, C. Barreneche, M. E. Navarro, Y. Ding, *Renewable Energy* **2020**, 156, 1244.
[11] B. Pomeroy, *Sol. Energy* **1979**, 23, 513.
[12] OECD/NEA Nuclear Science Committee Working Party on Scientific Issues of the Fuel Cycle Working Group on Lead-bismuth Eutectic, *Handbook on Lead-bismuth Eutectic Alloy and Lead Properties, Materials Compatibility, Thermal-hydraulics and Technologies*, OECD Publishing, Paris **2015**.
[13] J. Pacio, T. Wetzel, *Sol. Energy* **2013**, 93, 11.
[14] K. Niedermeier, Doctoral Thesis, KIT Scientific Reports 7755, KIT Scientific Publishing, **2019**.
[15] F. Müller-Trefzer, K. Niedermeier, M. Daubner, T. Wetzel, *Appl. Therm. Eng.* **2022**, 213, 118619.
[16] J. L. Ronald, G. Ballinger, *Nucl. Technol.* **2004**, 147, 418.
[17] J. Zhang, N. Li, *J. Nucl. Mater.* **2008**, 373, 351.
[18] J.-B. Vogt, I. Proriot Serre, *Coatings* **2021**, 11, 53.
[19] M. Popovic, A. Bolind, Y. Aussat, A. Gubser, P. Hosemann, *J. Nucl. Mater.* **2019**, 523, 172.
[20] J. Coventry, J. F. Torres, Z. Kee, M. Vahabzadeh Bozorg, M. Taheri, A. Mojiri, J. Pye, S. Bell, G. Will, T. Steinberg, in *Proc. Asia-Pacific Solar Research Conf. Sydney*, Sydney, Australia 16–17 December, **2021**.
[21] K. Niedermeier, L. Marocco, J. Flesch, G. Mohan, J. Coventry, T. Wetzel, *Appl. Therm. Eng.* **2018**, 141, 368.
[22] Verein deutscher Ingenieure, *VDI-Wärmeatlas*, Springer, Berlin Heidelberg **2013**.
[23] W. van Antwerpen, C. G. du Toit, P. G. Rousseau, *Nucl. Eng. Des.* **2010**, 240, 1803.
[24] A. Palacios, L. Cong, M. Navarro, Y. Ding, C. Barreneche, *Renewable Sustainable Energy Rev.* **2019**, 108, 32.
[25] S. Saha, B. Sharma, S. Kumar, G. Sahu, Y. Badhe, S. Tambe, B. Kulkarni, *Fuel* **2007**, 86, 1594.
[26] Schott Rohrglas GmbH, DURAN - Röhren, Kapillaren und Stäbe aus Borosilicatglas 3.3. (brochure), Mitterteich, Germany **2013**.
[27] F. Nakamori, Y. Ohishi, H. Muta, K. Kurosaki, K.-I. Fukumoto, S. Yamanaka, *J. Nucl. Sci. Technol.* **2017**, 54, 1267.
[28] E. Kleinert, personal communication (Saint Gobain) **2020**.
[29] G. Mueller, G. Schumacher, A. Weisenburger, A. Heinzl, F. Zimmermann, T. Furukawa, K. Aoto, *Study on Pb-Bi Corrosion of Structural and Fuel Cladding Materials for Nuclear Applications (2)*, Japan Nuclear Cycle Development Institute **2005**, <https://jopss.jaea.go.jp/pdfdata/JNC-TY9400-2005-021.pdf>.
[30] H. J. T. Ellingham, *J. Soc. Chem. Ind.* **1944**, 63, 125.
[31] O. Kubaschewski, C. Alock, *Metallurgical Thermochemistry*, Pergamon Press, Oxford **1979**.
[32] A. K. Rivai, M. Takahashi, *Prog. Nucl. Energy* **2008**, 50, 560.

- [33] A. Covington, A. Woolf, *J. Nucl. Energy Part B Reactor Technol.* **1959**, 1, 35.
- [34] W. Köck, P. Paschen, *JOM* **1989**, 41, 33.
- [35] C. Schroer, *Guidelines for Corrosion Testing in Liquid Metals (Pb, LBE) Deliverable D3.4*, MATTER, Seventh Framework Programme **2014**.
- [36] X. Huang, B. Pang, X. Zhou, Y. Yin, *Front. Energy Res.* **2021**, 9, 735199.
- [37] L. L. Hench, *MRS Online Proc. Lib.* **1988**, 125, 189.
- [38] B. Bunker, *J. Non-Cryst. Solids* **1994**, 179, 300.
- [39] R. Christenhusz, L. Reimer, *Z. Angew. Phys* **1967**, 23, 397.
- [40] J. I. Goldstein, D. E. Newbury, J. R. Michael, N. W. Ritchie, J. H. J. Scott, D. C. Joy, *Scanning Electron Microscopy and X-ray Microanalysis*, Springer, New York, NY **2017**.
- [41] C. Gumiński, *Int. J. Mater. Res.* **1990**, 81, 105.
- [42] S. Yatsenko, *Gallium. Interaction with Metals; Gallii. Vzaimodeistvie s Metallami*, Izdatel'stvo Nauka, Moscow **1974**.
- [43] W. Cook, *Oak Ridge National Lab. (No. ORNL-2391)*, Oak Ridge National Lab. (ORNL), Oak Ridge, TN **1960**.
- [44] J. J. Gangler, *J. Am. Ceram. Soc.* **1954**, 37, 312.
- [45] P. Auerkari, *VTT Res. Notes 1792*, Julkaisija – Utgivare, Finland **1996**.
- [46] S. Tuurna, A.-P. Nikkilä, T. Mäntylä, *Key Eng. Mater.* **2001**, 206, 1923.
- [47] Verband der keramischen Industrie e.V., www.keramverband.de/brevier_engl/5/6/1/5_6_1_3.htm (accessed: March 2023).
- [48] R. Asher, D. Davies, S. Beetham, *Corros. Sci.* **1977**, 17, 545.
- [49] H. Bach, J. Duffy, *J. Non-Cryst. Solids* **1978**, 29, 77.
- [50] Mühlmeier GmbH & Co KG, https://www.muehlmeier.de/fileadmin/user_upload/DE/mahltechnik/produktinformation/muehlmeier_de_dp.pdf (accessed: January 2023).
- [51] J. Paillier, C. Mickel, P. F. Gostin, A. Gebert, *Mater. Charact.* **2010**, 61, 1000.
- [52] Mühlmeier GmbH & Co. KG, https://www.muehlmeier.de/fileadmin/user_upload/DE/mahltechnik/produktinformation/muehlmeier_de_alox_z90_c92_k92.pdf (accessed: January 2023).
- [53] N. Louet, M. Gonon, G. Fantozzi, *Ceram. Int.* **2005**, 31, 981.
- [54] S. C. Whipkey, Doctoral Thesis, Alfred University **2020**
- [55] CeramTec, *Datasheet Steatite C220*, CeramTec GmbH, Chemical Applications Division, Marktredwitz, Germany **2019**.
- [56] L. Perfler, L. Peyker, M. Hörtnagl, N. Weinberger, C. Pichler, R. Traxl, R. Lackner, *Mater. Des.* **2022**, 218, 110704.
- [57] E. Vela, M. Peiteado, F. García, A. Caballero, J. Fernández, *Ceram. Int.* **2007**, 33, 1325.
- [58] D. Hülsenberg, *Keramik*, Springer, Berlin, Heidelberg **2014**.
- [59] Final Advanced Materials GmbH, www.final-materials.com/de/index.php?controller=attachment&id_attachment=91 (accessed: January 2023).
- [60] S. Hodgson, J. Cawley, M. Clubley, *J. Mater. Process. Technol.* **1999**, 92–93, 85.
- [61] W. C. Butterman, W. R. Foster, *Am. Mineral.* **1967**, 52, 880.
- [62] Saint-Gobain, Zirpro, *Rimax Technical Data Sheet*, SEPR - Saint-Gobain Zirpro, Le Pontet Cedex, France **2020**.
- [63] Informationszentrum Technische Keramik (IZTK) in cooperation with the member companies of the professional group Technische Keramik im Verband der Keramischen Industrie e.V., *Brevier Technische Keramik*, Fahner Verlag, Lauf **2003**.
- [64] M. Burghartz, H. Matzke, C. Léger, G. Vambenepe, M. Rome, *J. Alloys Compd.* **1998**, 271–273, 544.
- [65] H. Matzke, V. Rondinella, T. Wiss, *J. Nucl. Mater.* **1999**, 274, 47.
- [66] B. Arnold, *Zirconium Oxide Versus Aluminium Oxide-Zircon, Zirconium, Zirconia - Similar Names, Different Materials*, Springer Berlin, Heidelberg **2022**.